UCLA
UCLA Electronic Theses and Dissertations

Title
Graphene-Based Surface Plasmon-Polaritons for Terahertz Applications

Permalink
https://escholarship.org/uc/item/51r9m1zc

Author
Gu, Xuefeng

Publication Date
2013

Peer reviewed|Thesis/dissertation

UNIVERSITY OF CALIFORNIA

Los Angeles

Graphene-Based Surface Plasmon-Polaritons

for Terahertz Applications

A thesis submitted in partial satisfaction

of the requirement of the degree

Master of Science in Electrical Engineering

by

Xuefeng Gu

2013

ABSTRACT OF THE THESIS

Graphene-Based Surface Plasmon-Polaritons for Terahertz Applications

by

Xuefeng Gu

Master of Science in Electrical Engineering

University of California, Los Angeles, 2013

Professor Jia-Ming Liu, Chair

In this thesis, we focus on graphene-based surface plasmon-polaritons at terahertz frequencies and their possible applications. The primary motivation is to efficiently couple free-space terahertz radiation into an ultra-compact and low-loss waveguide. Characteristics of surface plasmon-polaritons on monolayer and double-layer graphene are first re-derived and reviewed. Then we propose two novel waveguide structures: graphene-metal structure and graphene-wrapped fibers. Possible modes that can be supported by the structures are analyzed and how to excite them is addressed. Also, promising applications are briefly described. Our work reveals that graphene-metal structure is a good starting point for exploration of both new physics and innovative devices, and that graphene-wrapped fibers can also be of substantial interest as the quality of graphene is improved.

The thesis of Xuefeng Gu is approved.

Tatsuo Itoh

Benjamin Williams

Jia-Ming Liu, Committee Chair

University of California, Los Angeles

2013

Table of Contents

List of Figures

Acknowledgement

I would like to first pay tribute to my advisor, Professor Jia-Ming Liu, who guided me throughout my research with incisive advices. Thanks to my committee members, Professor Itoh and Professor Williams for their helpful comments. Also, thanks to my friends in the Photonics Research Laboratory, with whom I have spent good time working together. Special thanks to I-Tan Lin for his helpful discussion and cooperation in my research that leads to certain parts of this thesis.

My deepest gratitude finally goes to my family for their encouragement and constant support.

CHAPTER 1

Introduction

Terahertz (THz) radiation has attracted tremendously increasing research interest during the past few decades. High-power sources, efficient detectors, and low-loss waveguides for THz applications are being developed extensively [1–6]. Among those interesting but challenging research topics, how to efficiently couple THz radiation into a compact and low-loss waveguide, especially in THz integrated devices, is an active area.

Due to the limit of diffraction, a moderate confinement of the THz wave can be achieved only when the size of the waveguide is comparable to the THz wavelength [7, 8]. This results in incredibly large device dimensions (~ 0.3 mm for 1 THz), making integration very difficult. At optical frequencies, this problem is resolved with the aid of surface plasmon-polaritons (SPPs) – the strong coupling between electromagnetic waves and plasma oscillations at the metal surface, to confine the light in a subwavelength scale [9–12]. But in the THz regime, metal behaves as a perfect electric conductor and only a small portion of the electromagnetic energy can reside in the metal, leading to a very loosely confined surface wave [13]. Researchers have suggested that metamaterials, artificially engineered electromagnetic materials, be exploited to manipulate microwave or even THz radiation in the subwavelength scale. Structures reported to date that can support SPP-like modes include periodically perforated metallic plates [14], hollow square-ended brass tubes [15], Sievenpiper mushrooms [16], and periodic patches [17]. However, most of these structures are

bulky and operate at microwave frequencies [14–16]. In the THz regime, the fabrication and active tuning of the SPP behavior become much more difficult.

Instead of metamaterials, we will focus on the use of graphene, a truly two-dimensional (2D) material consisting of honeycomb carbon atoms, to realize THz SPPs. Since its first discovery in 2004 by Geim and co-workers [18], graphene has attracted enormous attention for its extraordinary properties. Electrons close to the Dirac point traveling through the graphene carbon lattice exhibit a linear dispersion between its energy and momentum, and behave as massless Fermions [19–21]. This fact gives rise to many intriguing characteristics to graphene, such as quantum Hall effect [22, 23], unique conductivity [24], and extremely high mobility [25, 26]. Interesting electronic and photonic devices such as high-mobility field-effect transistors [27, 28], saturable absorbers [29], and ultrafast photodetectors [30] have been developed. Despite the rich electronic properties that have been widely investigated in recent years, we are primarily interested in the photonic properties of this novel 2D material.

Most photonic characteristics of graphene can be derived from its optical conductivity, defined as J/E, where J is the current density (in A/m for 2D materials) and E is the electric field. In general, the overall conductivity is contributed by two parts, the intraband conductivity and the interband one, and can be modeled, using relaxation time approximation, as [24, 31]:

$$\sigma = \sigma_{\text{intra}} + \sigma_{\text{inter}}$$

$$= i\frac{e^2 k_B T}{\pi \hbar^2 \left(\omega + i\tau_1^{-1}\right)}\left[\frac{\mu}{k_B T} + 2\ln\left(e^{-\frac{\mu}{k_B T}} + 1\right)\right] + i\frac{e^2}{4\pi\hbar}\ln\left[\frac{2|\mu| - \hbar\left(\omega + i\tau_2^{-1}\right)}{2|\mu| + \hbar\left(\omega + i\tau_2^{-1}\right)}\right] \quad (1.1)$$

Here, e is the electron charge, $\hbar$ is the reduced Plank constant, k_B is the Boltzmann constant, T is the temperature, ω is the optical frequency, μ is the chemical potential, and τ_1 and τ_2 are the relaxation times of intraband and interband scatterings, respectively. Note that the interband part is valid only when $\hbar\omega, |\mu| \gg k_{\mathrm{B}}T$, which is generally the case at room temperature at visible and infrared frequencies. At visible and infrared frequencies, the interband conductivity dominates, and graphene exhibits a constant conductivity of $e^2/(4\hbar)$. This means that a single sheet of graphene can absorb 2.3 % of the incident light across a large frequency band. Experiments have verified this theoretical prediction and also shown that the absorption increases linearly with the number of layers of graphene for less than $\sim$ 5 layers [32]. In the THz region (0.1–10 THz), on the other hand, the optical conductivity is dominated by the intraband contribution, and is tunable via variation of the chemical potential. It is important to note that, the phenomenological intraband scattering time, τ_1, in Eq. (1.1) has accounted for all scattering mechanisms including carrier-carrier scattering, impurity scattering, and phonon scattering, etc. In reality, τ_1 depends in a nontrivial way on many parameters such as temperature, carrier density, impurity density, and the substrate on which the graphene sheet is placed. However, we shall not consider the complicated dependence of τ_1 on these parameters. Instead, unless otherwise stated, we take $\tau_1 = 0.6$ ps, which corresponds to a mobility of 30,000 cm^{2}V^{-1}s^{-1} for μ = 0.2 eV (carrier density $2.9 \times 10^{12} / \mathrm{cm}^2$). This scattering time is realizable under current experimental conditions [24], and much longer scattering time has been used to theoretically investigate the SPP behavior of graphene [31, 33]. A typical plot of the

intraband conductivity versus frequency for $\mu = 0.2$ eV, $\tau_1 = 0.6$ ps , and $T = 300$ K is shown in Fig. 1.1. One feature that needs to be remarked is that for a certain frequency range, graphene conductivity has a positive imaginary part and a much smaller real part, which corresponds to a negative effective permittivity with small loss. As we shall see later, negative permittivity is essential for the support of SPP waves.
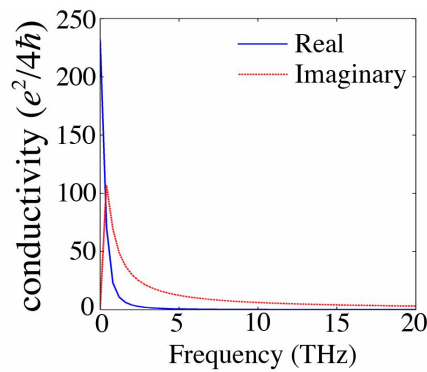
Figure 1.1 Intraband conductivity of graphene at THz frequencies.

So what are the advantages of graphene for THz SPP applications? First, the ultimately thin material can support highly confined THz waves, promising ultracompact THz integrated devices. Second, the loss of graphene-based SPP waveguide, characterized by the intraband scattering rate, is only limited by the quality of graphene, which is continuously being improved with the development of fabrication technology. Third, as aforementioned, the THz behavior of graphene can be actively tuned through variation of its chemical potential, and the switching speed is expected to be very fast as a result of its monolayer thickness and unique band structure. It is therefore easy to understand the exponentially increasing number of papers that are published on graphene-based THz plasmonics [34]. For example, plasmonic modes on both monolayer and double-layer graphene have been

investigated by several authors [35–38]. Also, many experiments have been reported to verify the existence of such modes. Ju. *et al.* provided the first experimental observation of plasmon response in graphene microstructures [39]. Fei et al. reported the first observation of plasmons at the interface between graphene and silicon dioxide (SiO2) [40]. Chen and coworkers recorded a real-time imaging of the plasmonic modes in tapered graphene nanostructures using near-field scattering microscopy [41]. These pioneering works have conclusively verified the existence of graphene-based plasmons, paving the way for various practical applications.

The outline of this thesis is as follows. In Chapter 2, we briefly derive and review the THz SPP modes supported by monolayer and double-layer graphene to lay the foundation of the rest of the thesis. In Chapter 3, a novel graphene-based THz SPP waveguide, namely graphene-metal plasmonic waveguide, is presented. The mode characteristics, including dispersion, confinement, and loss are first discussed. The most exciting feature of our waveguide is that the mode can be easily and efficiently excited with a normally incident beam if narrow periodic slits with an appropriate periodicity are created in the metal layer. Important factors that affect the excitation such as the slits periodicity and the duty factor are examined in details. Possible applications are also described. We suggest in Chapter 4 that, a graphene-wrapped fiber can support both fiber modes and SPP modes, and these two modes can be converted from one to another using properly designed fiber gratings. Finally, the conclusion and outlook are addressed in Chapter 5.

CHAPTER 2

Surface Plasmon-Polaritons in Monolayer and Double-Layer Graphene

We shall in this chapter briefly re-derive and review the basic properties of the SPP modes on monolayer and double-layer graphene to get an insight into our own structures presented in Chapter 3 and Chapter 4. For all the calculations below, we neglect the interband conductivity since all devices are operating at THz frequency and the loss due to interband transitions is small.

2.1 SPPs in Monolayer Graphene

We consider the structure depicted in Fig. 2.1, where a monolayer graphene is sandwiched between two half spaces filled with dielectric materials. The fields of the mode propagate along the z direction, exponentially decay along the $+x$ and $-x$ directions, and are homogeneous along the y direction ($\partial/\partial y = 0$). Both transverse electric (TE) and transverse magnetic (TM) modes can be supported by the structure, but as we shall see later, TE modes are loosely confined, and only TM modes are of interest for high-confinement applications.

Figure 2.1 The monolayer graphene structure which can support SPP modes.

For simplicity and without losing generality, we assume that the materials filling

the two half spaces are air. For the TM mode, with a propagation constant β, the fields are written as

$$H_y = Ae^{-\gamma x}e^{i\beta z} \tag{2.1}$$

$$E_x = \frac{\beta A}{\omega \varepsilon_0}e^{-\gamma x}e^{i\beta z} \tag{2.2}$$

$$E_z = -\frac{i\gamma A}{\omega \varepsilon_0}e^{-\gamma x}e^{i\beta z} \tag{2.3}$$

for $x > 0$, and

$$H_y = Be^{\gamma x}e^{i\beta z} \tag{2.4}$$

$$E_x = \frac{\beta B}{\omega \varepsilon_0}e^{\gamma x}e^{i\beta z} \tag{2.5}$$

$$E_z = \frac{i\gamma B}{\omega \varepsilon_0}e^{\gamma x}e^{i\beta z} \tag{2.6}$$

for $x < 0$, where ω is the THz radiation frequency, ε_0 is the electric permittivity of the air, $\gamma = \sqrt{\beta^2 - k_0^2}$ is the attenuation constant, k_0 is the free-space wave number, and A and B are undetermined coefficients. The boundary conditions are given by the continuity of E_z at $x = 0$ and Ampere's law:

$$E_z\big|_{x=0^+} = E_z\big|_{x=0^-} \tag{2.7}$$

$$H_y\big|_{x=0^+} - H_y\big|_{x=0^-} = \sigma E_z\big|_{x=0} \tag{2.8}$$

The dispersion relation of the mode is thus obtained:

$$\beta = k_0\sqrt{1-\left(\frac{2}{\sigma Z_0}\right)^2} \tag{2.9}$$

where $Z_0 = 120\,\pi\,\Omega$ is the free-space wave impedance. Similar to the SPP mode at the interface between a metal and a dielectric, the real part n'_β of the effective mode index, $n_\beta = \beta / k_0 = n'_\beta + in''_\beta$, is a measure of the mode confinement; the larger n'_β is,

the higher the confinement. By examining Eq. (2.9), we see that the resultant TM SPP

mode has a propagation constant much larger than k_0 if the conductivity of graphene

is purely imaginary with a positive imaginary part. Furthermore, the loss of the mode

is introduced by the real part of the conductivity. As technology advances, the loss of

the mode is expected to be substantially decreased. As justified in Chapter 1, unless

otherwise stated, in all calculations below, we assume an intraband relaxation time of

0.6 ps, which is a reasonable assumption for practical devices. We plot in Fig. 2.2 the

dispersion relation according to Eq. (2.9) when $T = 300$ K and $\mu = 0.2$ eV, in the

frequency band of 0 – 10 THz. A parabolic dependence of the propagation constant on

the frequency is observed in Fig. 2.2 (a). It is seen in Fig. 2.2 (b) that the real part of

the effective mode index can be up to 14.2, which leads to a deep-subwavelength

mode confinement. The loss is considerably high here, but as mentioned above it can

be reduced if the quality of graphene is improved.
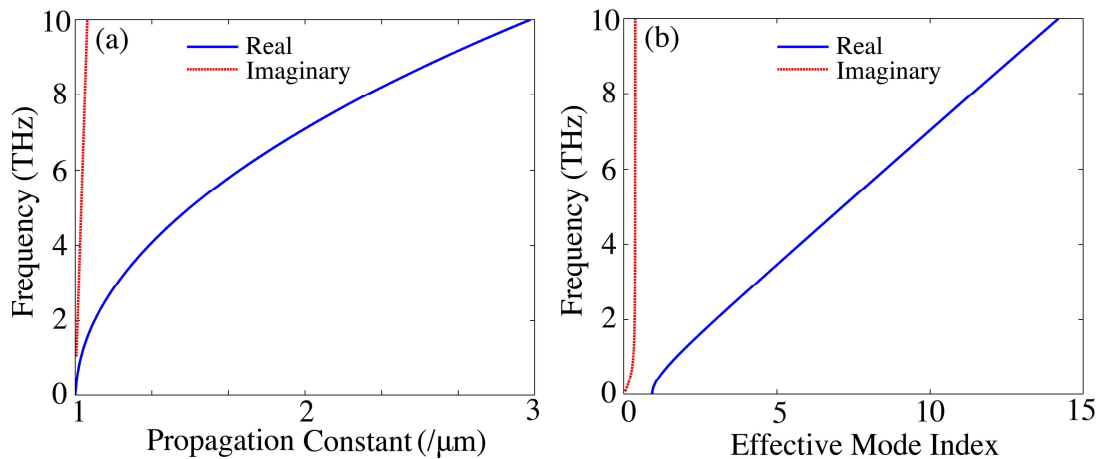
Figure 2.2 Dispersion of the monolayer graphene SPP mode. (a) Dispersion curve. (b) Effective mode index.

A similar analysis can be carried out for the TE mode, and the dispersion relation

is given by:

$$\beta = k_0 \sqrt{1 - \left(\frac{\sigma Z_0}{2}\right)^2} \qquad (2.10)$$

Unlike the TM SPP mode, the TE mode has a propagation constant close to k_0, which corresponds to a loosely confined mode. The fact that TE mode is much more loosely confined than the TM one is a general feature for all graphene-based SPP modes. From now on, we shall focus on the more interesting TM case in terms of high mode confinement.

There are many applications of the monolayer graphene SPP mode. Vakil *et al.* in 2011 proposed that one can exploit the ultra-compact profiles of TM SPP modes for flatland THz transformation optics devices [33]. One example is shown in Fig. 2.3, where a Luneburg lens is formed by biasing the regions marked by concentric circles at different voltages. Similar devices such as reflectors have also been reported [42, 43].
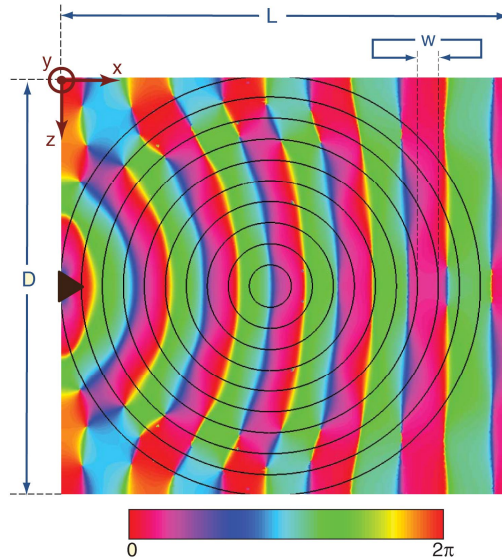
Figure 2.3 A 2D Luneburg lens realized by biasing the concentric circles at designed chemical potentials through an external voltage. $f = 30$ THz, $D = 1.5$ μm, $w = 75$ nm, and $L = 1.6$ μm. With permission from Ref [33].

2.2 SPPs in Double Layer Graphene

Besides the SPP mode supported by monolayer graphene, the mode supported by a pair of graphene sheets has also been discussed in the literature [37, 38].

The structure is illustrated in Fig. 2.4, where two graphene sheets are separated by a distance $2d$. Again, to avoid unnecessary complexity, we assume that all the dielectric materials are air, and two sheets of graphene have identical conductivities.
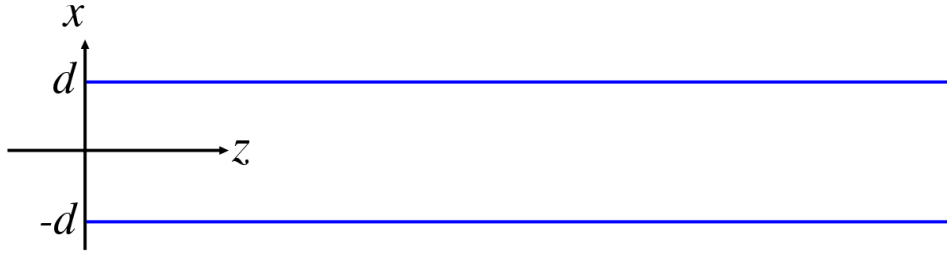
Figure 2.4 The double-layer graphene structure which can support SPP modes.

The magnetic fields are written as

$$H_y = Ae^{-\gamma x}e^{i\beta z} \tag{2.11}$$

for $x > d$,

$$H_y = \left(Be^{-\gamma x} + Ce^{\gamma x}\right)e^{i\beta z} \tag{2.12}$$

for $-d < x < d$, and

$$H_y = De^{\gamma x}e^{i\beta z} \tag{2.13}$$

For $x < -d$. Here, $\gamma = \sqrt{\beta^2 - k_0^2}$ is the attenuation constant and A, B, C and D are undetermined coefficients. The x- and z-components of the electric field can be obtained with equations similar to Eqs. (2.2) – (2.3) and Eqs. (2.5) – (2.6). By applying boundary conditions similar to those expressed in Eqs. (2.7) and (2.8), one can obtain the dispersion relations of the double-layer graphene SPP mode:

$$-1 = \left(1 + \frac{i\sigma\gamma}{\omega\varepsilon_0}\right)\tanh(\gamma d) \qquad (2.14)$$

for the even mode, and

$$-1 = \left(1 + \frac{i\sigma\gamma}{\omega\varepsilon_0}\right)\coth(\gamma d) \qquad (2.15)$$

for the odd mode. These two equations cannot be solved analytically. And since the characteristics of SPP modes supported by double-layer graphene are not the main concern of this thesis, we next look into the dispersion relations, assuming that graphene is lossless ($\tau \rightarrow \infty$, $T = 10$ K), to get a basic idea about the mode. The dispersion relations of both even and odd modes at a given frequency of 6 THz are plotted as a function of d in Fig. 2.5 for $\mu = 0.2$ eV. It is clear that the even mode has a larger propagation constant than the odd one, and it reaches an anomalously high value when the graphene-graphene spacing is extremely small. However, we should note that this will never happen since graphene cannot be lossless in reality and the properties of graphene will be altered if two sheets of graphene are placed too close to each other. It is also seen that the two curves for even and odd modes merge at large graphene-graphene spacings. This is expected because as the spacing increases, each sheet of graphene cannot see the effect of the other, and the SPP modes become the monolayer graphene SPP mode that has been discussed in Section 2.1. Coupled-mode theory can be employed to further understand this behavior. When the distance between the two graphene sheets is not too small, the coupled-mode theory provides a good estimate of the coupling behavior of the two modes, and this was utilized to couple SPP mode from one sheet of graphene to the other.
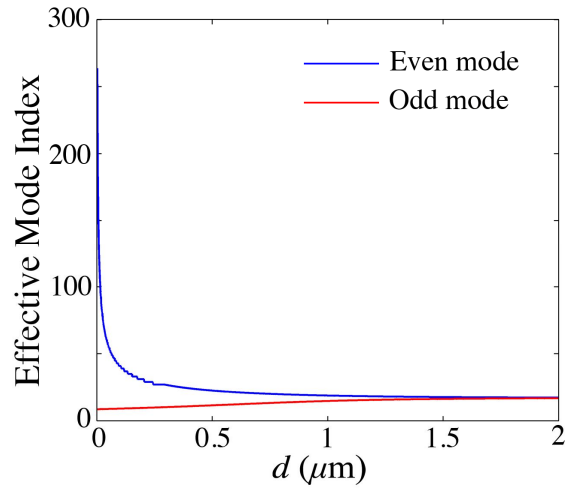
Figure 2.5 Dispersion of even and odd SPP modes on double-layer graphene structure. $\mu = 0.2$ eV and $f = 6$ THz.

We have so far discussed the SPP modes in monolayer and double-layer graphene structures. The physics of SPPs is described and the tools to analyze the mode are also developed. However, the SPP modes discussed above are difficult to excite in experiments. In Chapter 3, SPPs based on graphene-metal hybrid structure is proposed and an easy way to excite the mode is suggested.

CHAPTER 3

SPPs in Graphene-Metal Structures

In this chapter, we propose a novel graphene-metal hybrid structure which can support highly confined SPP modes.

3.1 SPP Modes in the Structure

The structure of the graphene-metal hybrid waveguide is schematically illustrated in Fig. 3.1, where graphene and metal are separated by a thin dielectric spacer with a permittivity of ε. The fields of the mode propagate along the $+z$ direction and exponentially decay away from the graphene into the air along the $+x$ direction. Both TE and TM SPP modes can be supported, but the TE mode is almost not confined, and only the TM one is highly confined with a much larger propagation constant than in free space. We shall in the following restrict our discussion on the TM SPP mode.
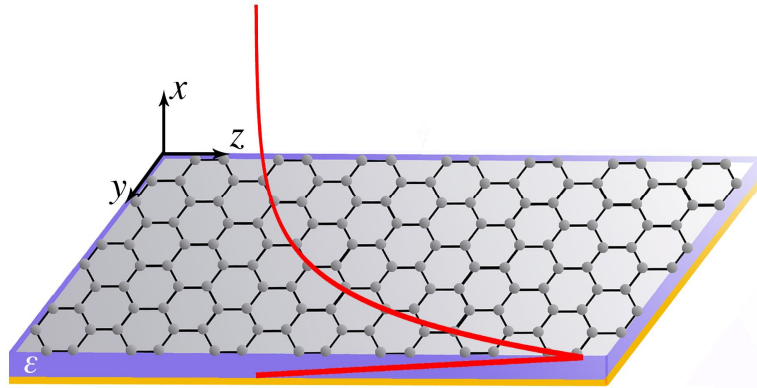
Figure 3.1 Schematic illustration of the graphene-metal SPP waveguide. Graphene (top) and metal (bottom) are separated by a dielectric spacer. The red curve represents a typical E_z distribution as a function of x.

The fields of the SPP are written as:

$$H_y = Ae^{-\gamma_1 x}e^{i\beta z} \tag{3.1}$$

$$E_x = \frac{\beta A}{\omega \varepsilon_0} e^{-\gamma_1 x} e^{i\beta z} \tag{3.2}$$

$$E_z = -\frac{i\gamma_1 A}{\omega \varepsilon_0} e^{-\gamma_1 x} e^{i\beta z} \tag{3.3}$$

for $x > 0$, and

$$H_y = \left(B e^{\gamma_2 x} + C e^{-\gamma_2 x} \right) e^{i\beta z} \tag{3.4}$$

$$E_x = \frac{\beta}{\omega \varepsilon} \left(B e^{\gamma_2 x} + C e^{-\gamma_2 x} \right) e^{i\beta z} \tag{3.5}$$

$$E_z = \frac{i\gamma_2}{\omega \varepsilon} \left(B e^{\gamma_2 x} - C e^{-\gamma_2 x} \right) e^{i\beta z} \tag{3.6}$$

for $-d < x < 0$. Here,

$$\gamma_1 = \sqrt{\beta^2 - k_0^2} \tag{3.7}$$

and

$$\gamma_2 = \sqrt{\beta^2 - \frac{\varepsilon}{\varepsilon_0} k_0^2} \tag{3.8}$$

are the attenuation constants in the air and in the dielectric, respectively. The boundary conditions at $x = 0$ are similar to those discussed in Chapter 2:

$$E_z \big|_{x=0^+} = E_z \big|_{x=0^-} \tag{3.9}$$

$$H_y \big|_{x=0^+} - H_y \big|_{x=0^-} = \sigma E_z \big|_{x=0} \tag{3.10}$$

but another boundary condition has to be enforced to account for the metal at $x = -d$. A good choice is to model the metal, typically gold or silver, as a perfect electric conductor (PEC). This is approximately the case for THz frequencies, and it is exactly why metal cannot support highly confined THz SPP modes. Then we have another boundary condition:

$$E_z \big|_{x=-d} = 0 \tag{3.11}$$

Combining Eqs. (3.9) through (3.11), we can obtain the dispersion relation of the

graphene-metal SPP mode:

$$-\frac{\gamma_1\varepsilon}{\gamma_2\varepsilon_0}=\left(1+\frac{i\sigma\gamma_1}{\omega\varepsilon_0}\right)\tanh\left(\gamma_2 d\right) \tag{3.12}$$

which, together with Eqs. (3.7) and (3.8) can be solved to obtain the mode

characteristics such as effective index, loss, field distribution, and energy distribution.

Let us first make several interesting observations on Eq. (3.12). First, we note

that when $\varepsilon = \varepsilon_0$, it reduces to the dispersion of the even double-layer graphene SPP

mode, as expressed in Eq. (2.14). This can be understood from the image theorem of

electromagnetics. We can imagine that if a PEC is inserted into the middle of the

double-layer graphene waveguide (i.e., the *y-z* plane in Fig. 2.4), the field distribution

of the even mode is not going to be changed. Though our structure can be intuitively

understood in this way, the introduction of metal indeed has its advantages; for

example it makes the excitation much easier and more efficient than the double-layer

case. Second, one may note that when the graphene-metal spacing *d* is very large,

such that $\tanh(\gamma_2 d) \approx 1$, Eq. (3.12) reduces to the dispersion relation $\varepsilon_2/\gamma_2 + \varepsilon_0/\gamma_1 + i\sigma/\omega$

$= 0$, which is the dispersion relation of the SPP mode supported by a monolayer

graphene alone. Finally, we should note that the real part of graphene conductivity has

to be positive for the mode to exist. Otherwise, the real parts of two sides of Eq. (3.12)

would have different signs.

Assuming that the dielectric is silicon dioxide (SiO_2, $\varepsilon = 3.9\,\varepsilon_0$), we give in Figs.

3.2(a) and (b) a typical plot of the dispersion relation of the graphene-metal SPP mode,

for different values of graphene-metal separation *d*. Other relevant parameters are as

follows: $\mu = 0.2$ eV, $T = 300$ K, and $\tau_1 = 0.6$ ps. As expected, at frequencies higher

than 6 THz, the curves for $d = 1$ μm and $d = 5$ μm merge. This is a direct consequence

of the high confinement of the mode at $f > 6$ THz, when the plasmon mode supported

by the monolayer graphene is highly confined so that it cannot "see" the effect of the

metal at a distance larger than 1 μm. For a given separation between graphene and

metal, as the frequency increases the real and imaginary parts of the effective index

each initially exhibits a monotonically decreasing behavior and then increases

monotonically after reaching a minimum. (For separations of 8 nm and 50 nm, the

minimum of n''_β is reached at frequencies higher than 10 THz, which is not shown in

Fig. 3.2(b).) There is a frequency range between the two minima where the loss

decreases while the confinement increases, a characteristic not observed in traditional

SPP modes at a metal-dielectric interface.
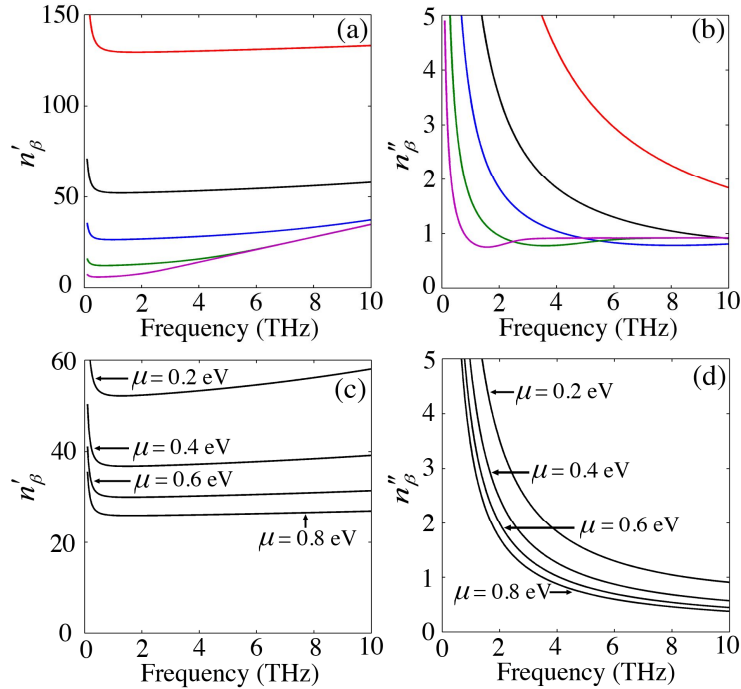

Figure 3.2   Dispersion of the graphene-metal SPP mode. (a) and (b): Real and imaginary parts of the mode index at a fixed chemical potential of $\mu = 0.2$ eV (carrier density $n = 2.9 \times 10^{12} / cm^2$) for different graphene-metal spacing: $d = 8$ nm (red), 50 nm (black), 200 μm (blue), 1 μm (green), and 5 μm (purple). (c) and (d): Real and imaginary parts of the

mode index at a fixed graphene-metal spacing of d = 50 nm for different chemical potentials.

Figures 3.2(c) and (d) show how the mode index evolves with the variation in the chemical potential for a given d = 50 nm. It is clear that the mode confinement as well as the loss decreases monotonically with increasing chemical potential, as is typically the case for single- and double-layer graphene plasmon waveguides. We can see from these results that a highly confined low-loss propagating plasmon mode is possible when the frequency is high and the separation between graphene and metal is relatively large, at a low chemical potential. If the intraband electron relaxation time is increased to 100 ps for a significantly low scattering rate, achievable in very pure graphene or at very low temperatures [44], the plasmon mode at 10 THz can be confined within $\lambda_0/100$, where λ_0 is the free-space terahertz wavelength, with a loss of only 0.6 dB/λ_0 when the graphene-metal separation is 8 nm and the chemical potential is 0.2 eV. Due to the tight confinement by the deep-subwavelength mode cross-sectional area, the fields will be extremely strong even with a moderate power.

3.2 Excitation of the SPP Mode by Narrow Periodic Slits

Because the propagation constant of graphene-metal SPP mode is much larger than the free-space wavenumber, and the field distribution is so different from free-space modes, it is not possible to efficiently excite the mode either through direct THz illumination or end-fire coupling configuration. Even worse, the well established Otto and Kretschmann coupling techniques at optical frequencies cannot be employed because one cannot find a THz prism with such high refractive index. Therefore, it is extremely difficult to excite graphene-based SPP modes. This is the reason why there

have not yet been many experimental reports on graphene-based SPPs so far. The only experimental works we can find to date are Refs. [40, 41, 45]. Using nanoscopy, Fei *et al.* were able to observe the SPP mode excited at the interface between graphene and SiO$_2$ [45]. However, the system is complicated and the excitation efficiency is not estimated. An easier and more controllable way to excite the graphene-based SPP modes remains absent.

We address in this section the most notable feature of our graphene-metal SPP waveguide: the mode can be easily and efficiently excited with normally incident THz beam if narrow periodic slits of an appropriate periodicity are created in the metal layer. The configuration that will be examined below is depicted in Fig. 3.3, where a sheet of graphene covers, at a distance *d* filled with a dielectric material, a periodic metallic grating with a periodicity of *Λ* and a duty factor of *ξ*. The idea stems from the fact that if a TM wave is incident upon a metal with narrow slits, wave vectors much larger than the free-space wavenumber will be generated in the vicinity of the slits. We therefore anticipate that if the periodicity of the slits is properly chosen, such that *2πq/Λ*, where *q* is an integer, matches the propagation constant of the SPP mode, the energy of the incident beam would be resonantly coupled to the SPP mode. Our prediction is verified by full-wave simulation using COMSOL Multiphysics, a commercial software based on the finite element method (FEM). We try to obtain the field distribution in the *x-z* plane, assuming that fields are homogeneous along the *y* direction. Two cases are considered: *d* = 50 nm and *d* = 8 nm. The thickness of the substrate is assumed to be 1 *μ*m. In practice, the substrate is much thicker than 1 *μ*m,

but the wave characteristics can be easily derived from the transfer matrix method. 30-nm thick gold is used for the metal. Floquet boundary condition is enforced to mimic the periodicity in the *z* direction.
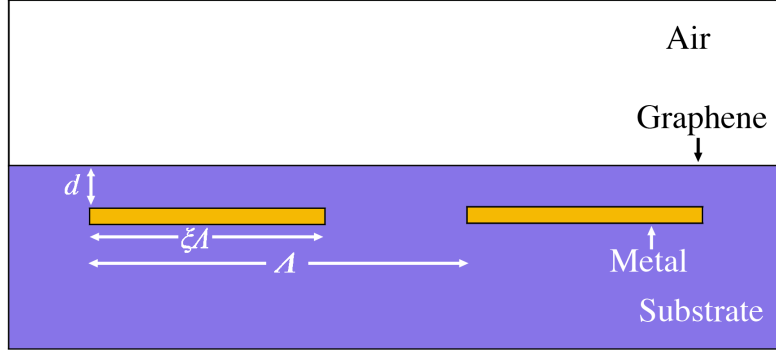
Figure 3.3   Illustration of the metallic grating structure that is used to excite the graphene-metal SPP mode. Only two periods are shown here. The periodicity of the metallic grating is Λ and the duty factor is ξ.

The absorption, $A = 1 - (T + R)$, where T and R respectively are the reflectance and transmittance of the structure, is a measure of the coupling efficiency. Let us first examine a typical example at 6 THz for a graphene chemical potential of $\mu = 0.2$ eV and graphene-metal spacing of $d = 50$ nm, where the plasmon mode wavelength is found to be $\lambda_P = 0.915$ μm. The absorption as a function of the grating period Λ when the duty factor is fixed at $\xi = 0.98$ is plotted in Fig. 3.4, where periodic resonance peaks close to $\Lambda/\lambda_P = 1, 2, 3, 4$, and 5 can be identified, corresponding to the first five orders of coupling between the incident wave and the plasmon mode. The positions of those peaks deviate from multiple times of λ_P, especially for higher-order couplings. We shall show in Section 3.3 that this is a result of structural dispersion introduced by the periodic structure. We show in Fig. 3.5(a) the electric field distribution in the *x-z* plane for the first-order coupling. Note that a standing wave pattern is formed because two contra-propagating SPP modes are excited. The simulated field decay rate into the

air, $\gamma_1 = 6.87 \ \mu m^{-1}$, is in excellent agreement with the theoretically calculated value.

Also, notice from Fig. 3.4 that the coupling becomes inefficient when the grating period deviates slightly from the absorption peaks, and the resonance linewidth is the smallest for the first-order coupling. As a comparison, the electric field distribution for $\Lambda/\lambda_P = 1.5$ is given in Fig. 3.5(b). It is clearly seen that the mode field is not as strong as that in Fig. 3.5(a) where the plasmon mode is efficiently excited.
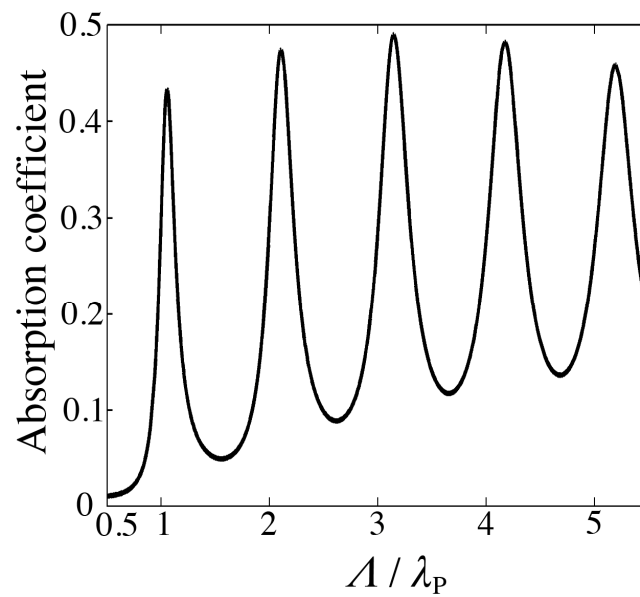
Figure 3.4 Absorption coefficient as a function of the periodicity when the duty factor is fixed at $\xi = 0.98$.
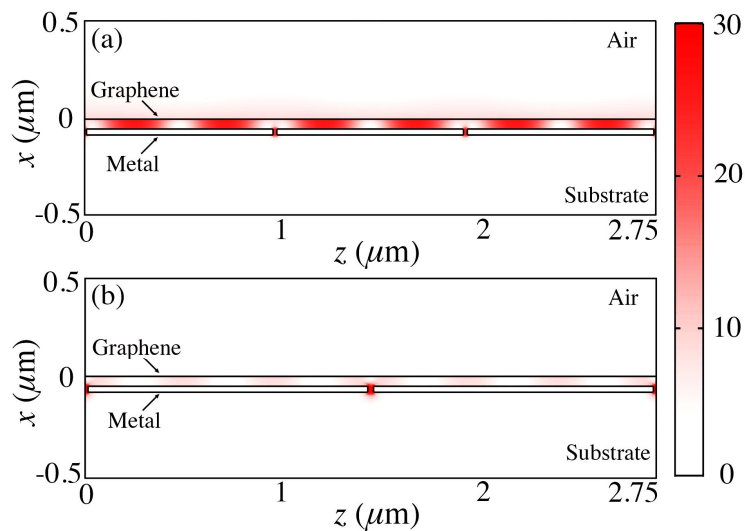
Figure 3.5 Normalized electric field distribution $|E/E_0|$ for (a) $\Lambda/\lambda_P = 1$ and (b) $\Lambda/\lambda_P = 1.5$.

Other factors such as the duty factor ξ of the metallic grating and the thickness of gold also affect the coupling efficiency. Basically, we tend to figure out their effects via numerical simulation because it is very difficult, if not impossible, to solve the problem analytically. As an example, Fig. 3.6 shows the coupling efficiency versus ξ for the first-order coupling, where two peaks at $\xi = 0.62$ and 0.99 are observed. The peak at $\xi = 0.99$ can be intuitively understood: on one hand, a high duty factor is necessary because the narrow slits are essential to excite the SPP mode; on the other hand, if the duty factor is too large (> 0.99 in the current case), the slits are too small for the incident beam to "see" them. But why is there an absorption peak at $\xi = 0.62$? The answer is the same as that of the question that why the absorption peaks in Fig. 3.4 deviate from multiple times of the SPP wavelength: the structural dispersion introduced by the periodic structure. This issue is discussed in details in the next section.
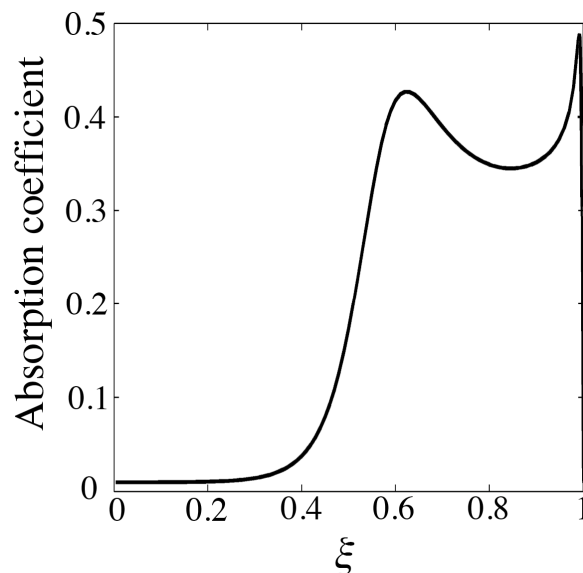
Figure 3.6   Absorption coefficient as a function of the duty factor ξ for the first-order coupling. Two peaks at $\xi = 0.62$ and 0.99 can be observed.

Another feature of the excitation configuration being discussed here is that the fields, not only in the vicinity of the periodic slits, but also across the whole graphene layer, is significantly enhanced when the SPP mode is efficiently excited. Based on the fact that the rate of energy being coupled to the SPP mode is equal to the energy dissipation rate in the waveguide structure, one can obtain the following expression for the maximum electric field enhancement:

$$\left| \boldsymbol{E} / \boldsymbol{E}_0 \right| \approx \sqrt{2\eta / \left(Z_0 \sigma' \right)} \coth\left(\beta d \right) \tag{3.13}$$

where $\eta \approx A$ is the coupling efficiency for this excitation scheme, $Z_0 = 120\pi\ \Omega$ is the wave impedance in free space, and σ' is the real part of the graphene conductivity. We show in Fig. 3.7 the simulated field enhancement at 8 THz for a graphene-metal separation of 8 nm when $\mu = 94$ meV. Note that the interband conductivity has also been included since the chemical potential is now low enough for the interband transitions to happen. It is seen that the field has a minimum enhancement of 16 times and a maximum field enhancement of 60 times, which is consistent with the results from our theoretical calculation. Note that this field enhancement is comparable to that reported in Ref. [44], but it can be obtained with a much shorter scattering time. The fact that such high field enhancement across the whole graphene sheet can be obtained merely through direct THz illumination might open up numerous nonlinear terahertz applications.
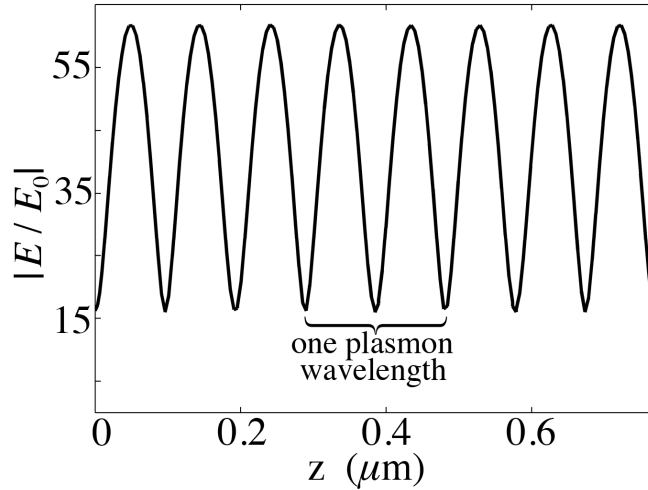
Figure 3.7   Simulated electric field enhancement at $x = 0^-$ beneath the graphene layer for graphene-metal spacing d = 8 nm, graphene chemical potential μ = 94 meV, and THz radiation frequency f = 8 THz.

3.3   Structural Dispersion of the Periodic Structure

We have noted two phenomena in the last section in the excitation of graphene-metal SPP modes with narrow periodic slits: 1) If the duty factor is fixed at ξ = 0.98, the absorption peaks occur when the periodicity $\varLambda$ is close to but not exactly equal to multiple times of the SPP wavelength. 2) If the periodicity of the metallic grating is fixed for the first-order coupling, there are two peaks when the duty factor is 0.62 and 0.99. We in this section use a mode-matching method to estimate and understand these two behaviors. In fact, instead of being coupled to the graphene-metal plasmon mode alone, the incident wave is coupled to an *effective* mode supported by the periodic structure. The graphene-metal plasmon mode is supported in regions with metal, whereas the monolayer graphene plasmon mode is supported in regions without metal. These two modes, combined with the boundary conditions between the two regions, determine the possible modes that can exist in the

periodic structure, among which the one of a minimum phase mismatch with the grating wavenumber is most likely to be excited. The idea is quantified in the following.

We denote the normalized field distribution H_y and E_x of the graphene-metal SPP mode with a propagation constant of β_1 as $\hat{H}_1$ and $\hat{E}_1$, respectively. Similarly, the normalized H_y and E_x of the SPP mode of a propagation constant β_2 supported by a monolayer graphene alone discussed in Section 2.1 are denoted as $\hat{H}_2$ and $\hat{E}_2$. As shown in Fig. 3.8, the fields in Region I are written as:

$$H_y = A\hat{H}_2 e^{i\beta_2 z} + B\hat{H}_2 e^{-i\beta_2 z} \tag{3.14}$$

$$E_x = A\hat{E}_2 e^{i\beta_2 z} - B\hat{E}_2 e^{-i\beta_2 z} \tag{3.15}$$

The fields in Region II are written as:

$$H_y = C\hat{H}_1 e^{i\beta_1 z} + D\hat{H}_1 e^{-i\beta_1 z} \tag{3.16}$$

$$H_y = C\hat{E}_1 e^{i\beta_1 z} - D\hat{E}_1 e^{-i\beta_1 z} \tag{3.17}$$

The fields in Region III are written as:

$$H_y = M\hat{H}_2 e^{i\beta_2 z} + N\hat{H}_2 e^{-i\beta_2 z} \tag{3.18}$$

$$E_x = M\hat{E}_2 e^{i\beta_2 z} - N\hat{E}_2 e^{-i\beta_2 z} \tag{3.19}$$
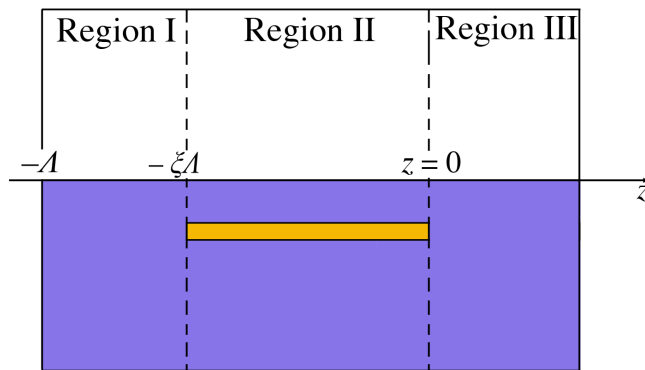

Figure 3.8 Structure for the analysis of structural dispersion introduced by the periodicity.

In fact, radiation modes have to be considered in Eqs. (3.14) through (3.19), but we ignore them here for the first-order estimate. For H_y and E_x to be continuous at $z = -\xi\Lambda$, we have:

$$A\hat{H}_2 e^{-i\beta_2\xi\Lambda} + B\hat{H}_2 e^{i\beta_2\xi\Lambda} = C\hat{H}_1 e^{-i\beta_1\xi\Lambda} + D\hat{H}_1 e^{i\beta_1\xi\Lambda} \tag{3.20}$$

$$A\hat{E}_2 e^{-i\beta_2\xi\Lambda} - B\hat{E}_2 e^{i\beta_2\xi\Lambda} = C\hat{E}_1 e^{-i\beta_1\xi\Lambda} - D\hat{E}_1 e^{i\beta_1\xi\Lambda} \tag{3.21}$$

Also, H_y and E_x have to be continuous at $z = 0$, which gives:

$$C\hat{H}_1 + D\hat{H}_1 = M\hat{H}_2 + N\hat{H}_2 \tag{3.22}$$

$$C\hat{E}_1 - D\hat{E}_1 = M\hat{E}_2 - N\hat{E}_2 \tag{3.23}$$

Another set of boundary conditions is given by the effective propagation mode:

$$e^{i\beta\Lambda}\left(Ae^{-i\beta_2\Lambda} + Be^{i\beta_2\Lambda}\right) = M + N \tag{3.24}$$

$$e^{i\beta\Lambda}\left(Ae^{-i\beta_2\Lambda} - Be^{i\beta_2\Lambda}\right) = M - N \tag{3.25}$$

where β is the effective propagation mode. Strictly, Eqs. (3.20) through (3.25) have to be satisfied for every point in the cross section, but this is impossible without the inclusion of radiation modes. If radiation modes are considered, integration equations with infinite number of unknowns have to be solved. Here, to the first order, we neglect the effect of radiation modes, and integrate appropriate forms of Eqs. (3.20) through (3.25) across the cross section (the x axis) to get a basic idea. As an example, multiplying both sides of Eq. (3.20) with $2\beta_1 H_1^* / (\omega\varepsilon)$ and integrating from $x = -d$ to ∞, we obtain:

$$\frac{2\beta_1 e^{-i\beta_2\xi\Lambda}P}{\omega}A + \frac{2\beta_1 e^{i\beta_2\xi\Lambda}P}{\omega}B - e^{-i\beta_1\xi\Lambda}C - e^{i\beta_1\xi\Lambda}D = 0 \tag{3.26}$$

where $P = \int_{-d}^{\infty} H_1^* H_2 / \varepsilon(x)\,\mathrm{d}x$. Similar equations can be obtained from Eqs. (3.21) through (3.23). These four equations, combined with Eqs. (3.24) and (3.25), provide a

system of six equations with six unknowns A, B, C, D, M and N. For a nontrivial

solution to exist, the determinant has to varnish, giving the following requirement on

the effective propagation constant β:

$$
\begin{vmatrix}
e^{i\beta\Lambda - i\beta_2\Lambda} & e^{i\beta\Lambda + i\beta_2\Lambda} & 0 & 0 & -1 & -1 \\
e^{i\beta\Lambda - i\beta_2\Lambda} & -e^{i\beta\Lambda + i\beta_2\Lambda} & 0 & 0 & -1 & 1 \\
\dfrac{2\beta_1 e^{-i\beta_2\xi\Lambda}P}{\omega} & \dfrac{2\beta_1 e^{i\beta_2\xi\Lambda}P}{\omega} & -e^{-i\beta_1\xi\Lambda} & -e^{i\beta_1\xi\Lambda} & 0 & 0 \\
\dfrac{2\beta_2 e^{-i\beta_2\xi\Lambda}P}{\omega} & -\dfrac{2\beta_2 e^{i\beta_2\xi\Lambda}P}{\omega} & -e^{-i\beta_1\xi\Lambda} & e^{i\beta_1\xi\Lambda} & 0 & 0 \\
0 & 0 & 1 & 1 & -\dfrac{2\beta_1 P}{\omega} & -\dfrac{2\beta_1 P}{\omega} \\
0 & 0 & 1 & -1 & -\dfrac{2\beta_2 P}{\omega} & \dfrac{2\beta_2 P}{\omega}
\end{vmatrix} = 0
$$

(3.27)

which can be solved for possible β. For a given set of periodicity Λ and duty factor ξ,

Eq. (3.27) either has a solution or does not have a solution. If there are β values which

can satisfy Eq. (3.27), we denote min $\{\beta, 2\pi/\Lambda - \beta\}$ as δ, the minimum phase mismatch.

The plot of δ as a function of the duty factor for the first-order coupling is given in

Fig. 3.9, from which two dips at $\xi = 0.72$ and 0.94 can be identified. Here, the

frequency is $f = 6\text{THz}$, the graphene-metal spacing is $d = 50$ nm, and the chemical

potential of graphene is $\mu = 0.2$ eV, to facilitate comparison with Fig. 3.4. Considering

that we have neglected the radiation modes, and did not consider the coupling

coefficient between the incident wave and the effective mode, this agreement between

semi-analytical results and simulation is reasonably good to provide an insight into

the complex problem.
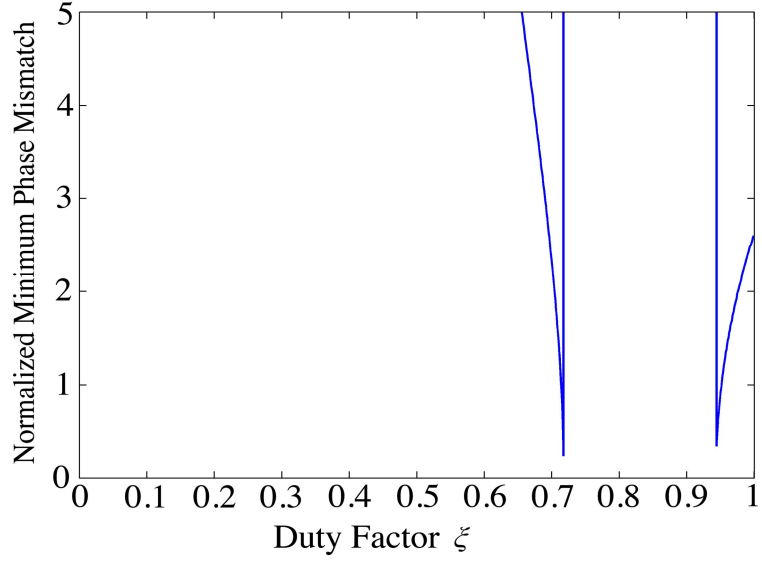
Figure 3.9 Minimum phase mismatch normalized to k_0 for the first-order coupling. $f = 6$ THz, $d = 50$ nm, and $\mu = 0.2$ eV.

The model just developed is employed to explain the deviation of absorption peaks from multiple times of λ_P that is observed in Fig. 3.4. We plot in Fig. 3.10 the minimum phase mismatch δ as a function of the periodicity Λ for a given duty factor of $\xi = 0.98$. It is observed that the phase mismatch dips deviate from multiple times of the SPP wavelength, in a way similar to what the absorption peaks do in Fig. 3.4.
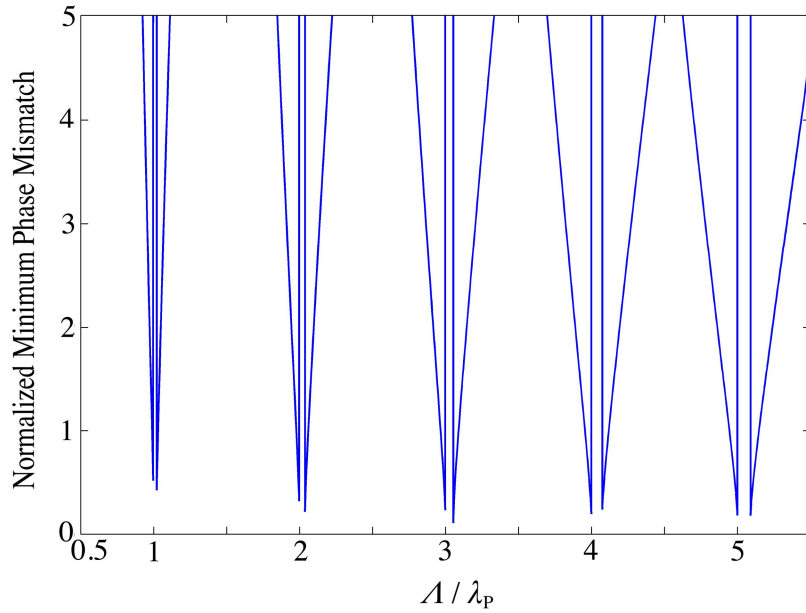

Figure 3.10   Minimum phase mismatch normalized to k_0 for a fixed duty factor of $\xi = 0.98$. $f = 6$ THz, $d = 50$ nm, and $\mu = 0.2$ eV.

We have in this section developed a first-order model to understand the structural dispersion of the periodic structure. This might be helpful in future device designs.

3.4   Applications of the Graphene-Metal SPPs

We are now ready to envision some interesting applications from our graphene-metal hybrid structure. The most straightforward application is THz filters. This can be observed by noting that the coupling efficiency from the incident wave to the SPP mode depends sensitively on the matching between the grating period and the SPP wavelength, which indicates that the proposed structure can be readily used as a terahertz filter. Also, combined with the tunability through variation of the chemical potential, the structure can be readily modified to operate as a THz modulator. In practical applications, the chemical potential can be tuned using an externally applied voltage across the graphene and the metal. Figure 3.11 shows how the structure can be used as a transmission-type modulator. The period of the metallic grating is $\Lambda = 0.915$ μm, the duty factor is $\xi = 0.98$, and the separation between graphene and metal is $d =$ 50 nm. As expected, there is a 4% transmission dip at 6 THz when the chemical potential is 0.2 eV, which is associated with the first-order grating coupling. As the chemical potential increases, the dip moves to a higher frequency. For example, for μ = 0.25 eV the dip occurs at 6.71 THz while the transmission at 6 THz is 22.7%. The modulation depth, defined as the ratio of the difference between high and low levels of transmission to the high level, at 6 THz is then 82.4%. Noting the simple relation $n = (|\mu|/\hbar v_f)^2/\pi$ between the carrier density and the chemical potential for graphene,

where $v_f \approx 10^6$ m/s is the Fermi velocity, we find that a change of $\Delta n = 1.65 \times 10^{12}$ cm^{-2} in the carrier density is sufficient to achieve such an extraordinary modulation performance. Actually, a modulation depth larger than 50% can be realized with a small change of only $\Delta n = 5 \times 10^{11}$ cm^{-2} in the carrier density. Specific design and optimization of the operating frequency and speed are beyond the scope of this thesis and will not be discussed further.
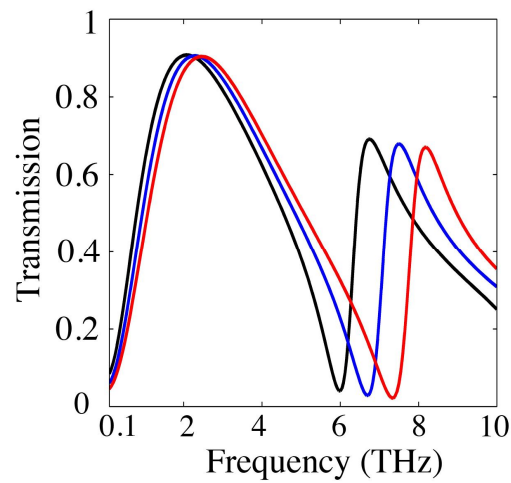
Figure 3.11 Tunable transmission through variation of the chemical potential for $\mu = 0.2$ eV (black), 0.25 eV (blue), and 0.3 eV (red).

In addition to THz filters and modulators, we also believe that the unique combination of metal (which can support optical SPPs) and graphene (which can support THz SPPs), together with the highly confined fields, are promising for optical-THz nonlinear interactions if some techniques to compensate for the loss can be developed in the future.

CHAPTER 4

Graphene-Wrapped Fibers

Up to this point, graphene-based SPP modes in monolayer graphene, double-layer graphene, and graphene-metal hybrid structures have been considered. We in this chapter describe a truly 3D structure – graphene-wrapped fibers. Figure 4.1 helps to understand the idea.

It is shown that if a fiber core of a radius a is wrapped with graphene, as depicted in Fig. 4.1(b), two different electromagnetic modes can be supported: the "fiber mode" and the SPP mode. The "fiber mode" results from the perturbation of the graphene wrapping, and has characteristics almost identical to those of fiber modes without graphene. On the other hand, the SPP mode takes advantage of the unique conductivity of graphene and does not exist in the absence of the graphene wrapping.

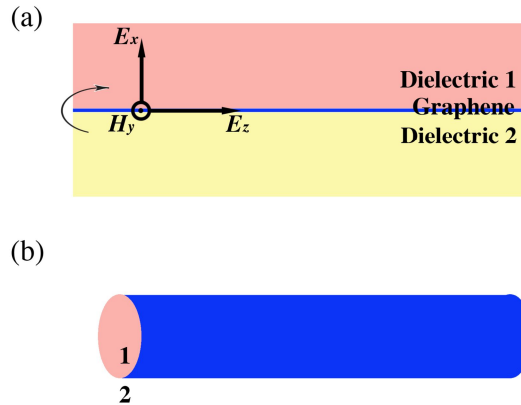Figure 4.1 Evolution of the structure from monolayer graphene to graphene-wrapped fibers. (a) A highly confined TM plasmon mode is supported by the 2D dielectric-graphene-dielectric structure. (b) By wrapping the structure with z being the axis, the structure in (a) becomes a "graphene-wrapped fiber", a real 3D structure.

4.1   Modes in the Structure

We focus on the TM modes with no angular dependence in the cylindrical

coordinate. The wave equation thus takes the form:

$$\left(k_i^2 - \beta^2\right)E_r = i\beta\frac{\partial E_z}{\partial r} \tag{4.1}$$

$$\left(k_i^2 - \beta^2\right)H_\theta = i\omega\varepsilon_i\frac{\partial E_z}{\partial r} \tag{4.2}$$

$$\frac{\mathrm{d}^2 E_z}{\mathrm{d}r^2} + \frac{1}{r}\frac{\mathrm{d}E_z}{\mathrm{d}r} + \left(k_i^2 - \beta^2\right)E_z = 0 \tag{4.3}$$

in each dielectric region. Here, $k_i^2 = \omega^2\mu_0\varepsilon_i$ and β is the propagation constant. Note that E_z is a function of r only.

Depending on whether $k_i^2 - \beta^2$ is positive or negative, the solution to Eq. (4.3) takes different forms. We call the modes "fiber modes" when $k_2 < \beta < k_1$ because they are similar to the modes in fibers without graphene; we call the modes "plasmon modes" when $\beta > k_1, k_2$ because they are directly the counterparts of the highly confined plasmon modes in 2D structures (Fig. 4.1(a)). The meaning of this nomenclature will become clearer later.

Let us first look into the fiber modes when $k_2 < \beta < k_1$. Eq. (4.3) is written as

$$\frac{\mathrm{d}^2 E_z}{\mathrm{d}r^2} + \frac{1}{r}\frac{\mathrm{d}E_z}{\mathrm{d}r} + \gamma_1^2 E_z = 0 \tag{4.4}$$

for $r < a$, and

$$\frac{\mathrm{d}^2 E_z}{\mathrm{d}r^2} + \frac{1}{r}\frac{\mathrm{d}E_z}{\mathrm{d}r} - \gamma_2^2 E_z = 0 \tag{4.5}$$

for $r > a$, where $\gamma_1^2 = \beta^2 - k_1^2$ and $\gamma_2^2 = k_2^2 - \beta^2$.

Thus, E_z can be written as:

$$E_z = \begin{cases} AJ_0\left(\gamma_1 r\right), & r < a \\ BK_0\left(\gamma_2 r\right), & r > a \end{cases} \tag{4.6}$$

where J_0 is the Bessel function of the first kind of order zero and K_0 is the modified

Bessel function of the second kind of order zero.

Expressing H_θ and E_r in terms of E_z using Eqs. (4.1) and (4.2), and

matching the boundary conditions:

$$E_z\big|_{r=a^+} = E_z\big|_{r=a^-} \tag{4.7}$$

$$H_\theta\big|_{x=a^+} - H_\theta\big|_{x=0^-} = \sigma E_z\big|_{x=0^+,0^-} \tag{4.8}$$

we can obtain the following dispersion relation of the fiber mode:

$$\frac{\varepsilon_1 J_0'\left(\gamma_1 a\right)}{\gamma_1 J_0\left(\gamma_1 a\right)} + \frac{\varepsilon_2 K_0'\left(\gamma_2 a\right)}{\gamma_2 K_0\left(\gamma_2 a\right)} = \frac{i\sigma}{\omega} \tag{4.9}$$

which has almost the same form as that of the modes in fibers without graphene,

$\dfrac{\varepsilon_1 J_0'\left(\gamma_1 a\right)}{\gamma_1 J_0\left(\gamma_1 a\right)} + \dfrac{\varepsilon_2 K_0'\left(\gamma_2 a\right)}{\gamma_2 K_0\left(\gamma_2 a\right)} = 0$, except for the term $i\sigma/\omega$ on the right-hand side.

For a specific example, we use SiO_2 ($\varepsilon_1 = 3.9\ \varepsilon_0$) as the fiber core and air ($\varepsilon_2 = \varepsilon_0$)

as the material for dielectric 2. Also, $f = 6$ THz, $T = 300\ K$, $\mu = 0.2$ eV and lossless

graphene is assumed for simplicity. Varying the radius of the fiber core, we obtain

the dispersion relation of the fiber modes in the presence of graphene as a function

of the V number $V = \dfrac{2\pi a}{\lambda}\sqrt{n_1^2 - n_2^2}$, and the results for the modes of first three

orders are given in Fig. 4.2 in black curves. Also shown in Fig. 4.2 in red curves are

the dispersion curves for the corresponding fiber modes without graphene. It is seen

that the dispersion relations in the presence of graphene are almost identical to those

of the modes without graphene. This means that graphene only plays a minor role in

modifying the dispersion of modes in conventional fibers. The electric field

distribution of the TM_{01} mode when the fiber radius is 30 μm is shown in Fig. 4.3.
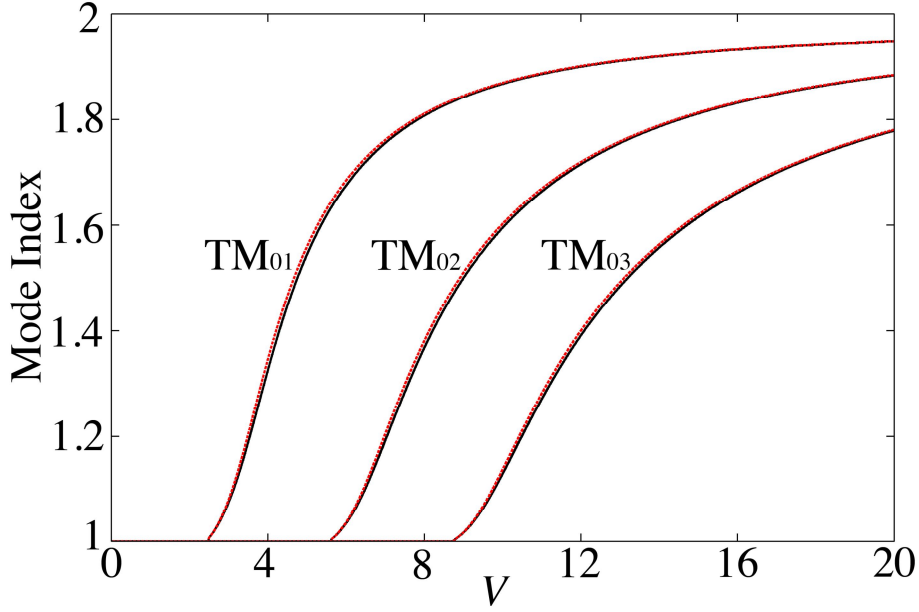
Figure 4.2 Dispersion of the first-three-order modes in graphene-wrapped fibers (black) and fibers without graphene (red curves). They are almost identical for the same mode order. At $f = 6$ THz, $T = 300$ K, and $\mu = 0.2$ eV.
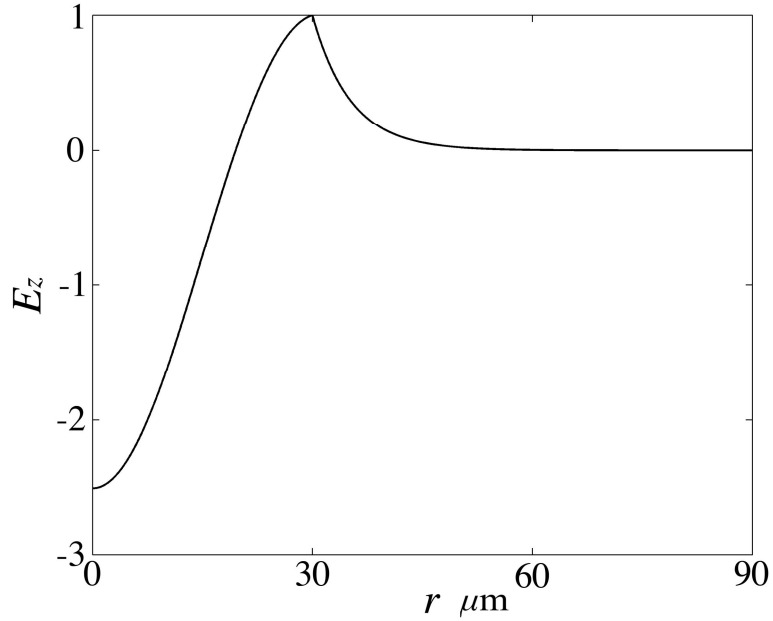
Figure 4.3 E_z field distribution at a radius of $a = 30$ μm.

In addition to the "fiber modes", graphene-wrapped fibers can also support a highly confined SPP mode under the condition that $\beta > k_1, k_2$. Now the electric field is written as:

$$E_z = \begin{cases} AI_0(\gamma_1 r), & r \leq a \\ BK_0(\gamma_2 r), & r > a \end{cases} \qquad (4.10)$$

where I_0 is the modified Bessel function of the first kind of order zero, and K_0 is the modified Bessel function of the second kind of order zero. Here, $\gamma_1^2 = \beta^2 - k_1^2$ and $\gamma_2^2 = \beta^2 - k_0^2$. The boundary conditions are:

$$E_z\big|_{r=a^-} = E_z\big|_{r=a^+} \tag{4.11}$$

$$H_\theta\big|_{r=a^+} - H_\theta\big|_{r=a^-} = \sigma E_z\big|_{r=a} \tag{4.12}$$

Then the dispersion relation of the SPP mode can be solved as:

$$\frac{\varepsilon_0 K_0{'}(\gamma_2 a)}{\gamma_2 K_0(\gamma_2 a)} - \frac{\varepsilon_1 I_0{'}(\gamma_1 a)}{\gamma_1 I_0(\gamma_1 a)} = \frac{i\sigma}{\omega} \tag{4.13}$$

Varying the fiber radius, we plot in Fig. 4.4 this dispersion relation at $f = 6$ THz. All other parameters are the same as those used above. Different from the dispersion shown in Fig. 4.2, the SPP mode being discussed here has no cutoff, as long as the dimension is large enough so that the conductivity model of graphene remains valid. It can be seen that as the radius of the fiber increases the dispersion approaches that of the mode supported by the 2D structure in Fig. 4.1(a). This behavior is expected because the SPP mode supported by the surface cannot "feel" the effect of the center of the fiber when the radius is large enough. We show in Fig 4.5 how the mode field distribution evolves as the fiber radius changes.
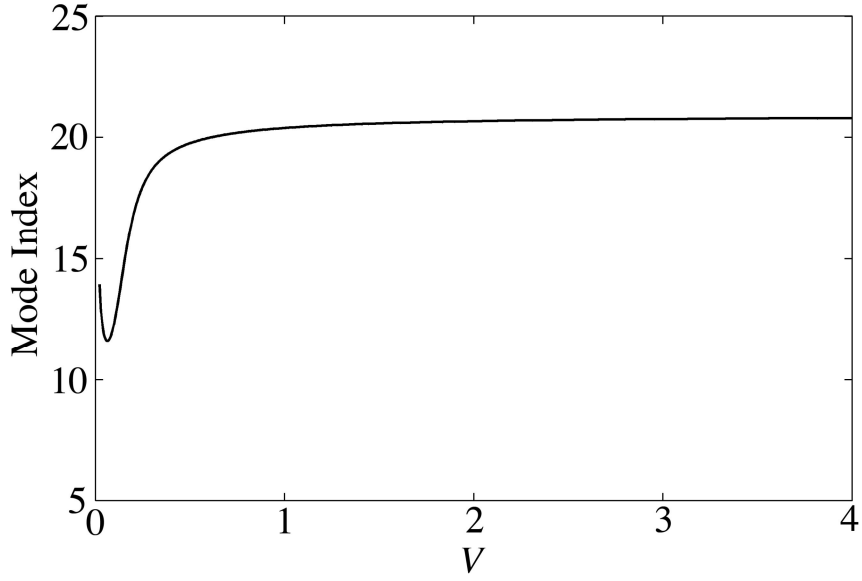
Figure 4.4 Dispersion of the SPP mode when f = 6 THz, T = 300 K, and μ = 0.2 eV. The mode has not cutoff. As the fiber radius increases (or equivalently, V increases) the mode index approaches that of the SPP mode supported by the dielectric-graphene-dielectric structure.
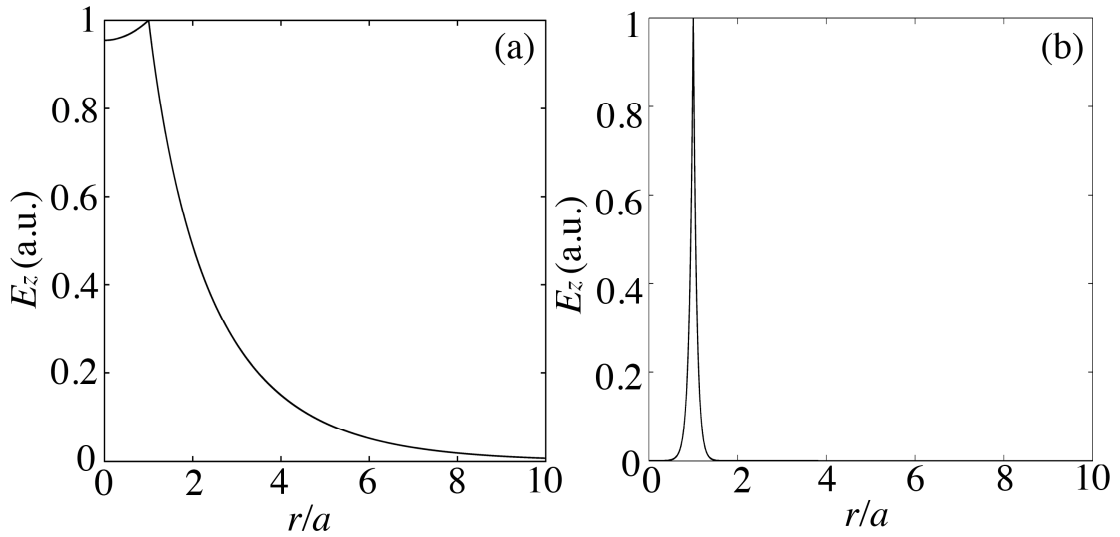
Figure 4.5 Electric field distributions for (a) a = 0.3 μm and (b) a = 5 μm. At f = 6 THz, T = 300 K, and μ = 0.2 eV.

4.2 Conversion from Fiber Modes to SPP Modes

We have in the last section discussed the possible modes in graphene-wrapped fibers: the "fiber modes" and the SPP modes. In this section, the coupling from one mode to the other through fiber gratings is considered, assuming that the graphene and dielectric material are lossless. This is not the case in practice, at least currently, but

the analysis presented here is still helpful because it provides an estimate of how long the fiber should be for the energy of the fiber modes to be completely transferred to the SPP mode. Then we would know the requirement on the loss of graphene and the dielectric materials.

We outline below the tedious procedure to find the coupling length for the maximum energy transfer to occur between the "fiber modes" and the SPP mode. First, to achieve the phase matching condition, a grating periodicity Λ that satisfies $2\pi/\Lambda = K$ where K is the phase mismatch between the two modes is chosen for first-order coupling. Second, the perturbation permittivity $\Delta\varepsilon$ is decided. Here, it is assumed that $\Delta\varepsilon = 0.01\varepsilon_0$ within the fiber core in the first half of the grating and $\Delta\varepsilon = -0.01\varepsilon_0$ within the fiber core in the second half of the grating. Then the normalized fields of the "fiber modes" and the SPP mode are used to find the coupling coefficient according to

$$\kappa_{fp}(z) = \omega\Delta\varepsilon(z)\int_0^{2\pi} d\theta \int_0^a \hat{E}_f^* \cdot \hat{E}_p r dr \qquad (4.14)$$

$$\kappa = \frac{1}{\Lambda}\int_0^\Lambda \kappa_{fp}(z) e^{-iKz} dz \qquad (4.15)$$

where the subscripts f and p denote the "fiber modes" and the SPP mode, respectively. The coupling length is found by

$$l = \frac{\pi}{2|\kappa|} \qquad (4.16)$$

Now let us consider a specific example in which energy is transferred from the fundamental TM mode, TM_{01} mode, to the SPP mode. When the frequency is 6 THz, the chemical potential is 0.2 eV, and the fiber radius is 30 μm, the propagation constants of the TM_{01} fiber mode and the SPP mode are $1.714k_0$ and $20.84k_0$,

respectively. The phase mismatch is thus $19.126k_0$ and the periodicity of the fiber grating is determined to be 2.6142 µm. After normalizing the field distribution of the two modes and using Eqs. (4.13) through (4.15) we obtain the coupling length $l =$ 3.55 cm. Since the plasmon mode has no cutoff, the graphene-wrapped fiber can then be tapered to a tip where the terahertz energy is extremely concentrated and the fields are significantly enhanced, which can be exploited for many applications such as sensing, imaging, etc.

However, this intriguing example has two major problems:

1) Loss. The fiber and graphene can never be lossless. Actually the loss of large-area graphene fabricated by chemical vapor deposition (CVD) is very high. This shortcoming might be circumvented in the future through improvement of the fabrication technique or some specific schemes to compensate for the loss.

2) It is hard to taper the graphene-wrapped fiber in fabrication. Also, the graphene conductivity change when it is tapered is not considered.

CHAPTER 5

Conclusion and Outlook

We have in this thesis comprehensively studied the highly confined SPP modes in various graphene-based structures. The ultimate aim of this investigation is to find an efficient way to excite the waveguide modes in a compact and low-loss THz waveguide, which is a key challenge in the THz research community.

In Chapter 2, a systematic approach to analyzing SPP modes supported by graphene-based structures is developed and the SPP modes supported by monolayer and double-layer graphene waveguides are briefly discussed. Though straightforward, this lays the foundation for further understanding of the two more complicated structures that are proposed thereafter.

A graphene-metal SPP waveguide is proposed in Chapter 3. The SPP mode supported by the structure has basically the same dispersion relation as the even mode of the double-layer graphene waveguide does. However, our structure has an advantage that cannot be achieved by any other structures reported to date: the mode can be easily and efficiently excited with a normally incident beam if narrow periodic slits of an appropriate periodicity are created in the metal. The excitation is due to the resonant coupling between the incident wave and the mode supported by the periodic structure. Furthermore, the structural dispersion introduced by the periodicity is examined using a first-order mode matching method, which produces a qualitatively good agreement with the full-wave simulation. Also, how the proposed structure can be readily used as a THz filter and an ultrafast THz modulator is briefly demonstrated.

Besides the approach to efficiently couple THz radiation to a deep-subwavelength waveguide that is described in Chapter 3, we in Chapter 4 considered another possibility: using graphene-wrapped fibers. Analysis shows that both "fiber modes" and SPP modes can exist in the structure, and the energy can be coupled from one to the other through properly engineered fiber gratings. A typical example reveals that the length of the fiber has to be as long as 3.55 cm for the complete energy transfer to happen. This is not practical with current graphene quality, and the feasibility thus relies to a large degree on the further advancement in graphene fabrication technology.

Some of the phenomena and devices presented in this thesis, for example the efficient excitation of graphene-metal SPP mode using narrow periodic slits in the metal, THz filters, and ultrafast THz modulators, may in the near future be observed or realized in experiments. Our future work will focus on practical devices based on these fundamental ideas. We believe that, with the advancement of graphene fabrication technology, our work in this thesis will pave the way for numerous innovative applications such as sensing, imaging, and communications.

References

1. M. Tonouchi, Nat. Photonics **1**, 97 (2007).

2. P. H. Siegel, IEEE T. Microw. Theory **3**, 910 (2002).

3. B. S. Williams, Nat. Photonics **1**, 517 (2007).

4. M. S. Vitiello, D. Coquillat, L. Viti, D. Ercolani, F. Teppe, A. Pitanti, F. Beltram, L. Sorba, W. Knap, and A. Tredicucci, Nano Lett. **12**, 96 (2012).

5. M. S. Vitiello, L. Viti, L. Romeo, D. Ercolani, G. Scalari, J. Faist, F. Beltram, L. Sorba, and A. Tredicucci, Appl. Phys. Lett. **100**, 241101 (2012).

6. C. Yeh, F. Shimabukuro, and P. H. Siegel, Appl. Optics **44**, 5937 (2005).

7. D. K. Gramotnev, and S. I. Bozhevolnyi, Nat. Photonics **4**, 83 (2010).

8. A. Andryieuski, A. V. Lavrinenko, and D. N. Chigrin, Phys. Rev. B **86**, 121108(R) (2012).

9. W. L. Barnes, A. Dereux, and T. W. Ebbesen, Nature **424**, 824 (2003).

10. W. Ding, S. R. Andrews, and S. A. Maier, Phys. Rev. A **75**, 063822 (2007).

11. E. Ozbay, Science **311**, 189 (2006).

12. S. A. Maier, and H. A. Atwater, J. Appl. Phys. **98**, 011101 (2005).

13. S. A. Maier, Plasmonics: Fundamentals and Applications (Springer, New York, 2007).

14. J. B. Pendry, L. Martin-Moreno, and F. J. Garcia-Vidal, Science **305**, 847 (2004).

15. A. P. Hibbins, B. R. Evans, and J. R. Sambles, Science **308**, 670 (2005).

16. M. J. Lockyear, A. P. Hibbins, and J. R. Sambles, Phys. Rev. Lett. **102**, 073901 (2009).

17. A. Ishikawa, S. Zhang, D. A. Genov, G. Bartal, and X. Zhang, Phys. Rev. Lett. **102**, 043904 (2009).

18. K. S. Novoselov, A. K. Geim, S. V. Morozov, D. Jiang, Y. Zhang, S. V. Dubonos, I. V. Grigorieva, and A. A. Firsov, Science **306**, 666 (2004).

19. A. H. Castro Neto, F. Guinea, N. M. R. Peres, K. S. Novoselov, and A. K. Geim, Rev. Mod. Phys. **81**, 109 (2009).

20. T. Ando, NPG Asia Mater. **1**, 17 (2009).

21. A. K. Geim, and K. S. Novoselov, Nat. Mater. **6**, 183 (2007).

22. K. S. Novoselov, Z. Jiang, Y. Zhang, S. V. Morozov, H. L. Stormer, U. Zeitler, J. C. Mann, G. S. Boebinger, P. Kim, and A. K. Geim, Science **315**, 1379 (2007).

23. V. P. Gusynin, and S. G. Sharapov, Phys. Rev. Lett. **95**, 146801 (2005).

24. P.-Y. Chen, and A. Alù, ACS Nano **5**, 5855 (2011).

25. K. I. Bolotin, K. J. Sikes, Z. Jiang, M. Klima, G. Fudenberg, J. Hone, P. Kim, and H. L. Stormer, Solid State Commun. **146**, 351 (2008)

26. C. R. Dean, A. F. Young, I. Meric, C. Lee, L. Wang, S. Sorgenfrei, K. Watanabe, T. Taniguchi, P. Kim, K. L. Shepard, and J. Hone, Nat. Nanotechnol. **5**, 722 (2010).

27. F. Schwierz, Nat. Nanotechnol. **5**, 487 (2010).

28. L. Britnell, R. V. Gorbachev, R. Jalil, B. D. Belle, F. Schedin, A. Mishchenko, T. Georgiou, M. I. Katsnelson, L. Eaves, S. V. Morozov, N. M. R. Peres, J. Leist, A. K. Geim, K. S. Novoselov, and L. A. Ponomarenko, Science **335**, 947 (2012).

29. G. Xing, H. Guo, X. Zhang, T. C. Sum, C. Hon, and A. Huan, Opt. Express **18**, 4564 (2010).

30. T. Mueller, F. Xia, and P. Avouris, Nat. Photonics **4**, 297 (2010).

31. S. A. Mikhailov, and K. Ziegler, Phys. Rev. Lett. **99**, 016803 (2007).

32. R. R. Nair, P. Blake, A. N. Grigorenko, K. S. Novoselov, T. J. Booth, T. Stauber, N. M. R. Peres, and A. K. Geim, Science **320**, 1308 (2010).

33. A. Vakil, and N. Engheta, Science **332**, 1291 (2011).

34. A. N. Grigorenko, M. Polini, and K. S. Novoselov, Nat. Photonics **6**, 749 (2012).

35. A. Y. Nikitin, F. Guinea, F. J. García-Vidal, and L. Martín-Moreno1, Phys. Rev. B **84**, 161407 (2011).

36. M. Jablan, H. Buljan, and M. Soljačić, Phys. Rev. B **80**, 245435 (2009).

37. E. H. Hwang, and S. D. Sarma, Phys. Rev. B **80**, 205405 (2009).

38. B. Wang, X. Zhang, X. Yuan, and J. Teng, Appl. Phys. Lett. **100**, 131111 (2012).

39. L. Ju, B. Geng, J. Horng, C. Girit, M. Martin, Z. Hao, H. A. Bechtel, X. Liang, A. Zettl, Y. R. Shen, and F. Wang, Nat. Nanotechnol. **6**, 630 (2011)

40. Z. Fei, G. O. Andreev, W. Bao, L. M. Zhang, A. S. McLeod, C. Wang, M. K. Stewart, Z. Zhao, G. Dominguez, M. Thiemens, M. M. Fogler, M. J. Tauber, A. H. Castro-Neto, C. N. Lau, F. Keilmann, and D. N. Basov, Nano Lett. **11**, 4701 (2011).

41. J. Chen, M. Badioli, P. Alonso-González, S. Thongrattanasiri, F. Huth, J. Osmond, M. Spasenović, A. Centeno, A. Pesquera, P. Godignon, A. Z. Elorza, N. Camara, F. J. García, R. Hillenbrand, and F. H. L. Koppens, Nature **487**, 77 (2012)..

42. A. Vakil, and N. Engheta, Opt. Commun. **285**, 3428 (2012).

43. H. J. Xu, W. B. Lu, Y. Jiang, and Z. G. Dong, Appl. Phys. Lett. **100**, 051903 (2012).

44. A. R. Davoyan, V. V. Popov, and S. A. Nikitov, Phys. Rev. Lett. **108**, 127401 (2012).

45. Z. Fei, A. S. Rodin, G. O. Andreev, W. Bao, A. S. McLeod, M. Wagner, L. M. Zhang, Z. Zhao, M. Thiemens, G. Dominguez, M. M. Fogler, A. H. Castro-Neto, C. N. Lau, F. Keilmann, and D. N. Basov, Nature **487**, 82 (2012).